

Dry reforming of methane in a stagnation-flow reactor using Rh supported on strontium-substituted hexaaluminate

Nicholas E. McGuire^a, Neal P. Sullivan^{a,*}, Olaf Deutschmann^b, Huayang Zhu^a, Robert J. Kee^a

^a Engineering Division, Colorado School of Mines, Golden, CO 80401, USA

^b Institute for Chemical Technology and Polymer Chemistry, Karlsruhe, Institute of Technology, Karlsruhe, Germany

ARTICLE INFO

Article history:

Received 8 October 2010

Received in revised form

30 December 2010

Accepted 6 January 2011

Available online 13 January 2011

Keywords:

Methane

Dry reforming

Rhodium

Hexaaluminate

Stagnation flow

Modeling

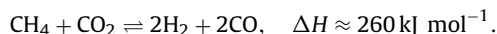
ABSTRACT

A combination of experiment and modeling is used to investigate catalytic reforming of methane with carbon dioxide (dry reforming) in a stagnation-flow reactor. The catalyst surface is a porous washcoat of rhodium supported on strontium-substituted hexaaluminate. The stagnation-flow configuration enables microprobe sampling of the compositional boundary layer adjacent to the catalyst surface. This configuration also enables efficient modeling the heterogeneous chemistry, coupled with convective and diffusive transport within the gas-phase boundary layer. The measurements provide new data that assist the fundamental understanding of methane dry reforming. The modeling incorporates an elementary reaction mechanism that was developed initially to represent catalytic partial oxidation and steam reforming. Representing the new dry-reforming measurements required modification of reaction rates for CO₂ and CH₄ interactions on the catalyst surface.

© 2011 Elsevier B.V. All rights reserved.

1. Introduction

It is well known that with appropriate catalysts, CO₂ can reform hydrocarbons to synthesis gas (H₂ and CO). For methane, dry reforming can be represented globally as



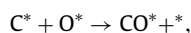
Because methane dry reforming produces a hydrogen-carbon ratio of two, the syngas is well suited for liquid-fuel synthesis. Thus, it may be possible to develop processes that reduce CO₂ (a greenhouse gas) and produce valuable liquid fuels via processes such as Fischer-Tropsch.

Rhodium is a good dry-reforming catalyst because of its high activity and low propensity for carbon formation [1,2]. The present effort considers Rh supported on strontium-doped hexaaluminates, which are stable at the high temperature needed for effective dry reforming [3].

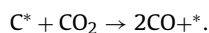
Optimization of processes and reactor geometries can be facilitated through the use of computational models that incorporate elementary reaction mechanisms. Compared to global reactions, detailed reaction mechanisms provide great flexibility in spanning the wide operating space between steam reforming, dry reforming,

partial oxidation, and autothermal reforming. Such modeling can provide design guidance for optimal reforming approaches. Thus, there is great value in improving the reaction mechanisms.

Elementary reaction mechanisms for dry reforming of methane have been previously developed for a range of possible catalysts. Bradford and Vannice published a comprehensive review of the dry reforming process, including mechanism development [4]. It is particularly interesting to understand the mechanisms by which surface carbon is oxidized. Rostrup-Nielsen and Bak-Hansen reported performance of methane dry reforming with various noble-metal catalysts [1]. They proposed a pathway that begins with the dissociative adsorption of methane, followed by the oxidation of surface carbon by surface oxygen,



where the * indicates a surface site or surface species. The primary source of surface oxygen in this pathway is the dissociative adsorption of CO₂. Similar pathways were proposed by Erdohelyi et al. [5], Efstathiou et al. [6], and Wei and Iglesia [7]. Mark and Maier proposed an alternative two-step pathway in which dissociatively adsorbed methane produces surface carbon that reacts with gas-phase CO₂ to produce CO [8]. That is,



More recently, Maestri et al. published a C₁ microkinetic model that incorporates dry-reforming pathways [9]. In their model the

* Corresponding author. Tel.: +1 303 273 3656; fax: +1 303 273 3602.
E-mail address: nsullivan@mines.edu (N.P. Sullivan).

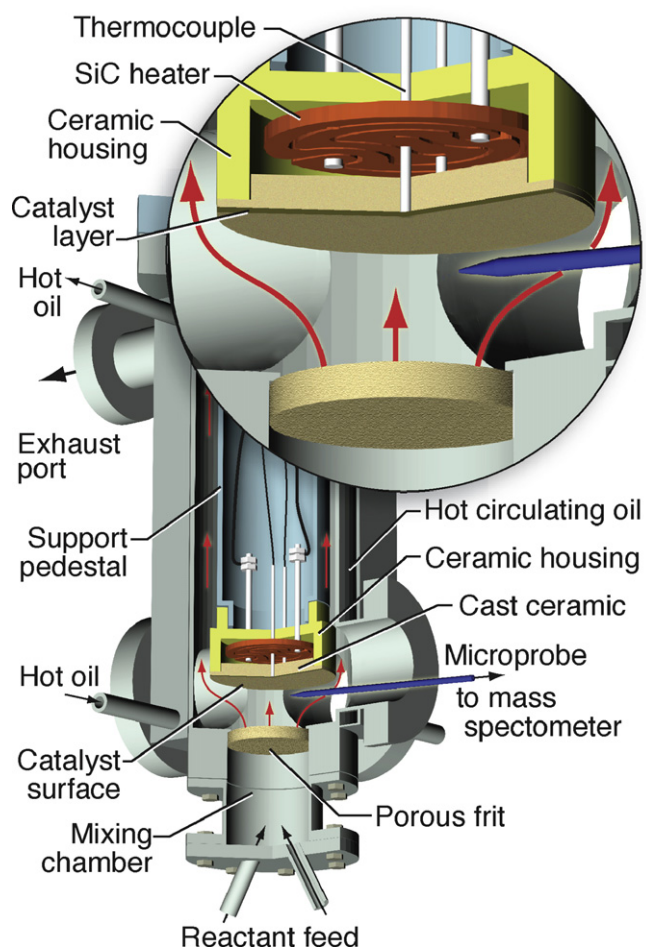
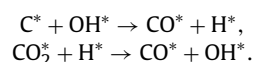


Fig. 1. Illustration of the stagnation-flow reactor. The inset highlights details around the catalytic surface.

oxidation of surface carbon occurs by reaction with adsorbed hydroxyl [10]. The adsorbed hydroxyl originates from the reaction of adsorbed CO_2 and dissociatively adsorbed H_2 :



The stagnation-flow reactor illustrated in Fig. 1 and introduced in a previous publication [3] is a useful tool for developing elementary reaction mechanisms. Stagnation flow has fluid-mechanical properties that enable measurement and modeling of the gas-phase boundary layer adjacent to the catalytic surface [3,11]. Such measurements are not available in practical reactor configurations (e.g., channel monoliths or porous foams). The stagnation-flow similarity creates a one-dimensional flow field where temperature and species profiles within the boundary layer do not vary with radial position. The one-dimensional nature facilitates computational modeling and evaluation of reaction mechanisms [12,13]. Although the stagnation flow has properties that are valuable in the laboratory, the configuration is not useful as a practical catalytic reactor. Nevertheless, the chemical information derived from the experiments can be applied via modeling to practical reactor configurations such as channel monoliths [14], ceramic-foam supported catalysts [15], or packed beds.

The primary objective of this work is to use a combination of stagnation-flow experiments and modeling to assist the development and validation of reaction chemistry using a Rh-based catalyst. Detailed reaction mechanisms developed by Deutschmann and colleagues [16–18] already incorporate the

elementary reactions that contribute to dry reforming, as well as partial oxidation and steam reforming. The mechanism used here was developed initially using a combination of theory and experiments spanning conditions for steam reforming and partial oxidation in monolith reactors [18]. Although the mechanism includes elementary steps for dry-reforming, it has not been specifically validated for such conditions. The present results show that modifications of CO_2 surface reaction rates are needed to represent the stagnation-flow measurements.

2. Experimental

2.1. Catalyst and surface preparation

In this work the rhodium catalyst is supported on strontium-substituted hexaaluminate ($\text{SrAl}_{11}\text{O}_{18}$), which is prepared using co-precipitation of appropriate nitrates. The hexaaluminate synthesis begins by mixing 3.14 g of $\text{Sr}(\text{NO}_3)_2$ (Sigma-Aldrich) with 61.3 g of $\text{Al}(\text{NO}_3)_3$ (Sigma-Aldrich), which are dissolved in 200 mL of de-ionized water. The resulting mixture is stirred and 5.0 M ammonium hydroxide is added until a pH between 7 and 8 is obtained. The mixture is then dried at 110°C and calcined at 1300°C . The resulting hexaaluminate support is in powder form.

After mixing the powder-form hexaaluminate (0.1 g) with aluminum hydroxide (11 mL), the solution is sprayed on to a pre-cast ceramic substrate (Cotronics Rescor 780) until a thickness of approximately $20\text{--}25\ \mu\text{m}$ is achieved. At thicknesses greater than approximately $20\ \mu\text{m}$ intraporal diffusion can limit access to the catalysts below the gas-phase interface [19]. After the hexaaluminate solution has been applied to the ceramic surface, the substrate is heated in a furnace to 550°C , which converts the aluminum hydroxide to alumina. The Rh metal is added via incipient-wetness impregnation using rhodium nitrate ($\text{Rh}(\text{NO}_3)_3$). Rh loadings of approximately 10 weight percent relative to the hexaaluminate are used. After Rh-addition the substrate is calcined in a furnace at 800°C for 1 h to convert the rhodium nitrate to rhodium oxide.

The substrate with catalyst coating is bonded to a pre-cast ceramic housing that contains the heater assembly. This assembly is then loaded into the stagnation-flow reactor (Fig. 1). Prior to measurements the catalyst is reduced from rhodium oxide to rhodium with a flow of 3.5 volume percent hydrogen in argon at 500°C for 3 h.

2.2. Physical characterization of catalyst and support

A JEOL 7000F microscope operated at 2.0 kV is used to obtain scanning electron micrographs. The secondary electron detector is used to evaluate the morphology in prepared catalyst samples.

Surface area for catalyst support powders is determined through the use of a Micromeritics Flowsorb II 2300 BET surface-area analyzer. The method used is single-point N_2 adsorption (ASTM D4567). Prior to BET surface-area measurements, the sample is degassed at a temperature of 300°C for 1 h.

Active metal surface area is quantified using the CO pulse-chemisorption method at 0°C . The hexaaluminate support powder is mixed with aluminum hydroxide and coated onto carrier particles until a thickness of approximately $20\ \mu\text{m}$ is achieved. The Rh metal is added to the sample via incipient-wetness impregnation using rhodium nitrate ($\text{Rh}(\text{NO}_3)_3$). The sample, including support and rhodium, is reduced in a flow of H_2 at 400°C prior to CO pulse chemisorption experiments. During the chemisorption experiments the reduced catalyst sample is exposed to $10\ \mu\text{L}$ pulses of CO at 4 min intervals until the active surface is completely covered in chemisorbed CO molecules. An adsorption stoichiometry of 1:1 between CO molecules and Rh surface atoms is assumed

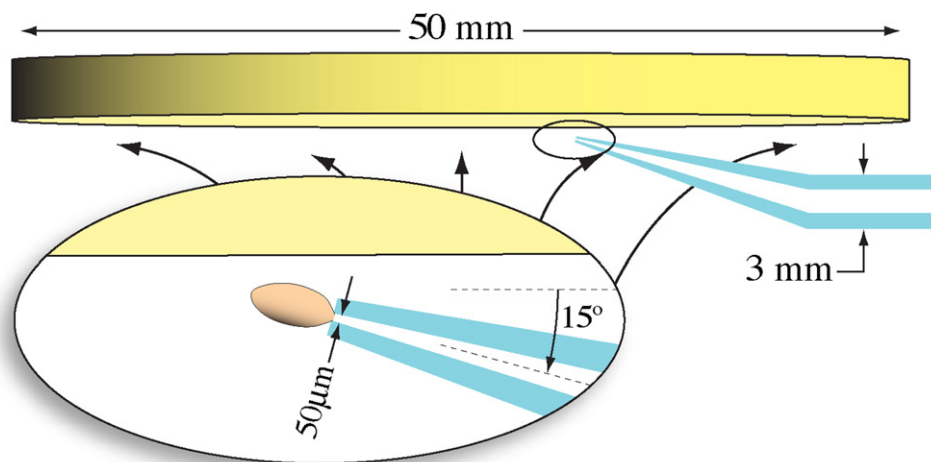


Fig. 2. Illustration of the quartz microprobe in relation to the stagnation surface.

[8]. Using this technique, the active surface area of a 10 wt% Rh/Sr-hexaaluminate catalyst is found to be approximately a factor of 56 greater than the geometric surface area.

2.3. Stagnation-flow reactor

Fig. 1 shows an illustration of the stagnation-flow reactor, which is fabricated from stainless steel [3]. During operation, room-temperature reactive gases (e.g., CO₂ and CH₄) enter from below and impinge upon the downward-facing heated catalyst surface. The catalyst surface is approximately 5 cm in diameter and the separation distance between the porous-frit gas inlet and the catalyst surface is approximately 1.6 cm. Mass-flow controllers maintain specified reactant flow rates. Elevated catalyst temperature (typically between 700 °C and 850 °C) is maintained using a SiC resistive heater (Morgan Advanced Ceramics) that is located directly above the pre-cast ceramic substrate. Two thermocouples are embedded in the cast-ceramic stagnation surface to measure the catalyst surface temperature. Hot oil circulates through the reactor housing to control wall temperature (≈60 °C), primarily to eliminate water condensation on the walls.

Gases are exhausted from the stagnation-flow reactor through an annular space by a vacuum pump. The pump maintains reactor pressure at 300 Torr. Sub-atmospheric reactor pressure serves to increase the boundary-layer thickness, which facilitates measurement of boundary-layer profiles. Gases such as CO₂ and CH₄ react on the catalyst surface, producing H₂ and CO. Because of diffusive and convective behaviors a boundary layer is formed adjacent to the surface. Composition profiles within the chemical boundary layer are measured via mass spectrometry, with samples drawn through a quartz microprobe that is positioned with a precision stepper motor.

The main tube of the quartz microprobe is 3 mm in diameter with the tip drawn to an outside diameter of 0.3 mm and bent 15° (Fig. 2). The bend angle is needed to position the tip very near the stagnation surface without interference from the relatively large main tube. The microprobe tip has a 50 μm opening and is positioned at a radial distance of 10 mm from the center of the stagnation surface. The probe can also be rotated approximately 45° around the probe axis, thus effectively reducing the tip angle relative to the catalyst surface. The probe tip is oriented such that it points toward the centerline of the axisymmetric stagnation flow. In this way, probe disturbance is reduced because the radially outward flow enters the probe volume before interacting with the probe itself.

2.4. Boundary-layer measurements

The quartz microprobe is initially positioned at a distance of approximately $z=0.1$ mm from the stagnation surface. Gases are sampled for four minutes, which is found to be sufficient time for the flow field to achieve steady-state operation. Sampled gases are sent to a quadrupole mass spectrometer (SRS RGA 200) for analysis. At the end of the four minute sampling period the quartz microprobe is moved an increment of 0.635 mm away from the previous measurement point. A boundary-layer profile typically consists of eight measurement points, spanning a distance of approximately 5 mm below the stagnation surface.

The quadrupole mass spectrometer is calibrated using a pre-mixed gas with known concentrations of CH₄, CO₂, CO, H₂ and Ar. Mass spectrometer signals for the gases of interest (H₂ at 2 amu, CH₄ at 15 amu, CO at 28 amu, O₂ at 32 amu, Ar at 40 amu, and CO₂ at 44 amu) are measured relative to Ar. The only signal overlap considered is the CO₂ contribution to the CO signal at 28 amu. Water vapor is not measured.

3. Computational model

The model is formulated as an axisymmetric stagnation-flow boundary-layer problem, which is well documented [11]. Briefly summarized, the governing equations can be stated as

$$\frac{d(\rho u)}{dz} + 2\rho V = 0, \quad (1)$$

$$\rho u \frac{dV}{dz} + \rho V^2 = -\Lambda_r + \frac{d}{dz} \left(\mu \frac{dV}{dz} \right), \quad (2)$$

$$\rho u c_p \frac{dT}{dz} = \frac{d}{dz} \left(\lambda \frac{dT}{dz} \right) - \sum_{k=1}^K \rho Y_k V_k c_{pk} \frac{dT}{dz} - \sum_{k=1}^K h_k W_k \dot{\omega}_k, \quad (3)$$

$$\rho u \frac{dY_k}{dz} = -\frac{d}{dz} (\rho Y_k V_k) + W_k \dot{\omega}_k \quad (k = 1, K_g), \quad (4)$$

$$p = \rho R T \sum_{k=1}^K \frac{Y_k}{W_k}. \quad (5)$$

In these equations the independent variable is the axial coordinate z . The dependent variables are the axial velocity u , the scaled radial velocity $V = v/r$ (v is the radial velocity and r is the radial coordinate), the temperature T , and the mass fractions Y_k . The

pressure-gradient eigenvalue is

$$\Lambda_r = \frac{1}{r} \frac{dp}{dr}. \quad (6)$$

The perfect-gas equation of state relates the pressure p , density ρ , temperature, and mass fractions, with R and W_k being the gas constant and molecular weights, respectively. Other variables include the mixture specific heat c_p , dynamic viscosity μ , and thermal conductivity λ . The variable $\dot{\omega}_k$ is the molar production rate of species k via gas-phase kinetics and h_k is the enthalpy of species k . Simulations that incorporate gas-phase chemistry (GRI-Mech 3.0 [20]) show that the effects of gas-phase chemistry are negligible for methane reforming at temperatures below 900 °C, thus they are excluded from the simulations presented here. As a limiting case, simulations were also run with the water-gas-shift reaction at equilibrium. Similarly, there is a negligible effect on the predicted boundary-layer species-profiles.

The species diffusion velocities are evaluated as

$$V_k = \frac{1}{X_k \bar{W}} \sum_{j \neq k} W_j D_{kj} \frac{dX_j}{dz} - \frac{D_k^T}{\rho Y_k T} \frac{dT}{dz}, \quad (7)$$

where X_j are mole fractions, \bar{W} is the mean molecular weight, D_{kj} are the ordinary multicomponent diffusion coefficients, and D_k^T are thermal diffusion coefficients.

Boundary conditions at the inlet (i.e., the porous frit shown in Fig. 1) are

$$u = U_{in}, \quad V = 0, \quad T = T_{in}, \quad Y_k = Y_{k,in}. \quad (8)$$

Boundary conditions at the catalytic stagnation surface are

$$u = 0, \quad V = 0, \quad T = T_s, \quad \rho Y_k V_k = F_{cat,geo} \dot{S}_k W_k. \quad (9)$$

The last condition above means that the diffusive flux of gas-phase species k at the surface is balanced by the net molar production rate of that species via catalytic kinetics (Table 1). Furthermore, the net production rate of surface-adsorbed species must vanish (i.e., $\dot{S}_k = 0$, ($k = 1, K_s$), where K_s is the number of surface species). Details about surface-kinetics formulation may be found in Kee et al. [11].

The boundary condition in Eq. (9) uses an effective area, $F_{cat,geo}$. Because the catalyst is dispersed as small particles in the porous support, the active catalyst area $A_{catalyst}$ is typically much greater than the geometric surface area $A_{geometric}$. This area ratio may be defined as

$$F_{cat,geo} = \frac{A_{catalyst}}{A_{geometric}}. \quad (10)$$

Due to stagnation-flow similarity the problem is mathematically an ordinary-differential-equation boundary-value problem. Following finite-volume discretization on an adaptive mesh network, the resulting nonlinear algebraic problem is solved using a hybrid Newton method [21]. The modeling results in this paper are computed using the Spin software, which is part of the Chemkin package [11,22,23].

4. Catalytic reaction mechanism

The heterogeneous reaction mechanism used in this work (Table 1) is a subset and modification of a mechanism recently published by Hartmann et al. [18] for the catalytic partial oxidation of iso-octane on rhodium. The subset is formed simply by eliminating all higher-hydrocarbon reactions (C_2 and above). The reduced C_1 mechanism consists of 42 irreversible elementary reactions involving 12 surface-adsorbed species and 6 gas-phase species. It should be noted that the mechanism was developed originally for Rh

Table 1
Surface reaction mechanism, modified from Hartmann et al. [18].

	Reaction	A^\dagger	E^\ddagger
1	$H_2 + * \rightarrow H^* + H^*$	1.0×10^{-2a}	0.00
2	$O_2 + * \rightarrow O^* + O^*$	1.0×10^{-2a}	0.00
3	$CH_4 + * \rightarrow CH_4^*$	8.0×10^{-3a}	0.00
4	$H_2O + * \rightarrow H_2O^*$	1.0×10^{-1a}	0.00
5	$CO_2 + * \rightarrow CO_2^*$	$4.8 \times 10^{-2a,c}$	0.00
6	$CO + * \rightarrow CO^*$	5.0×10^{-1a}	0.00
7	$H^* + H^* \rightarrow H_2 + Rh^{*+}$	3.0×10^{21}	77.80
8	$O^* + O^* \rightarrow O_2 + Rh^{*+}$	1.3×10^{22}	355.20
	θ_O^*		-280.0 ^b
9	$H_2O^* \rightarrow H_2O + *$	3.0×10^{13}	45.00
10	$CO^* \rightarrow CO + *$	3.5×10^{13}	133.40
	θ_{CO}^*		-15.0 ^b
11	$CO_2^* \rightarrow CO_2 + *$	4.1×10^{11b}	18.00 ^c
12	$CH_4^* \rightarrow CH_4 + *$	1.9×10^{14c}	25.10
13	$H^* + O^* \rightarrow OH^* + *$	5.0×10^{22}	83.70
14	$OH^* + * \rightarrow H^* + O^*$	3.0×10^{20}	37.70
15	$H^* + OH^* \rightarrow H_2O^* + *$	3.0×10^{20}	33.50
16	$H_2O^* + * \rightarrow H^* + OH^*$	5.0×10^{22}	106.40
17	$OH^* + OH^* \rightarrow H_2O^* + O^*$	3.0×10^{21}	100.80
18	$H_2O^* + O^* \rightarrow OH^* + OH^*$	3.0×10^{21}	171.8
19	$C^* + O \rightarrow CO^* + *$	5.2×10^{23}	97.90
20	$CO^* + * \rightarrow C^* + O^*$	2.5×10^{21}	169.00
21	$CO^* + O^* \rightarrow CO_2^* + *$	5.5×10^{18}	121.60
22	$CO_2^* + * \rightarrow CO^* + O^*$	3.0×10^{21}	171.8
23	$CO^* + H^* \rightarrow HCO^* + *$	5.0×10^{19}	108.90
24	$HCO^* + * \rightarrow CO^* + H^*$	3.7×10^{21}	0.00
	θ_{CO}^*		+50.0 ^b
25	$HCO^* + * \rightarrow CH^* + O^*$	3.7×10^{24}	59.50
26	$CH^* + O^* \rightarrow HCO^* + *$	3.7×10^{21}	167.50
27	$CH_4^* + * \rightarrow CH_3^* + H^*$	3.7×10^{21}	61.00
28	$CH_3^* + H^* \rightarrow CH_4^* + *$	3.7×10^{21}	51.00
29	$CH_3^* + * \rightarrow CH_2^* + H^*$	3.7×10^{24}	103.00
30	$CH_2^* + H^* \rightarrow CH_3^* + *$	3.7×10^{23}	44.10
31	$CH_2^* + * \rightarrow CH^* + H^*$	3.7×10^{24}	100.00
32	$CH^* + H^* \rightarrow CH_2^* + *$	3.7×10^{21}	68.00
33	$CH^* + * \rightarrow C^* + H^*$	3.7×10^{21}	21.00
34	$C^* + H^* \rightarrow CH^* + *$	3.7×10^{21}	172.80
35	$CH_4^* + O^* \rightarrow CH_3^* + OH^*$	1.7×10^{24}	80.34
36	$CH_3^* + OH^* \rightarrow CH_4^* + O^*$	3.7×10^{21}	24.27
37	$CH_3^* + O^* \rightarrow CH_2^* + OH^*$	3.7×10^{24}	120.31
38	$CH_2^* + OH^* \rightarrow CH_3^* + O^*$	3.7×10^{21}	15.06
39	$CH_2^* + O^* \rightarrow CH^* + OH^*$	3.7×10^{24}	114.50
40	$CH^* + OH^* \rightarrow CH_2^* + O^*$	3.7×10^{21}	36.82
41	$CH^* + O^* \rightarrow C^* + OH^*$	3.7×10^{21}	30.13
42	$C^* + OH^* \rightarrow CH^* + O^*$	3.7×10^{21}	136.00

[†] Arrhenius parameters for the rate constants written in the form: $k = A_{exp} \exp(-E/RT)$. The units of A are given in terms of moles, centimeters, and seconds. E is in kJ mol⁻¹.

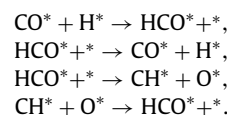
^a Sticking coefficient.

^b Coverage dependent activation energy. Detailed definition may be found in Kee et al. [11]

^c Modified rate parameter. Total available surface site density is $\Gamma = 2.72 \times 10^{-9}$ mol cm⁻².

dispersed on alumina washcoats; the present study uses Rh supported on Sr-doped hexaaluminate. Previous studies indicate that the identity of the support has little effect on the dry-reforming reaction rate over Rh catalysts [7,8].

Compared to earlier mechanisms for methane reforming and partial oxidation [16,17], the Hartmann et al. mechanism [18] includes the following reactions involving HCO* on the catalyst surface:



The implementation of the HCO* species is supported by TPSR and TR-FTIR experiments carried out by Yan et al. [24]. The present results show that these reactions are particularly important under dry-reforming conditions.

Table 2
Modified reaction rate parameters.

	Reaction	A^a	E (kJ mol ⁻¹)
5.	CO ₂ +* → CO ₂ *		
	Original [18]	$1.0 \times 10^{-0.5b}$	0.0
	Modified	$4.8 \times 10^{-0.2b}$	0.0
11.	CO ₂ * → CO ₂ +*		
	Original [18]	1.0×10^{13}	21.7
	Modified	4.1×10^{11}	18.0
12.	CH ₄ * → CH ₄ +*		
	Original [18]	1.0×10^{13}	25.1
	Modified	1.9×10^{14}	25.1

^a The units of A are moles, cm, s.^b Sticking coefficient

Applying the Hartmann et al. mechanism [18] to model the present dry-reforming conditions predicts nearly complete surface coverage by carbon, and hence no reforming activity. Thus, some mechanism modification is required. Sensitivity analysis provides specific clues regarding directions for modification with Reactions 5, 11, and 12 found to be very sensitive. Increasing the CO₂ adsorption rate (Reaction 5) and decreasing the desorption rate (Reaction 11) delivers more oxygen to the surface, which, through a series of reactions, serves to oxidize surface carbon and increase gas-phase CO production. Increasing the CH₄ desorption rate also serves to reduce the surface-carbon coverage. Table 2 shows the pre-exponential factors and activation energies in the original mechanism [18] and the altered parameters used in the present work. Model predictions using this modified mechanism are in good agreement with experimental data over a range of operating conditions.

The adsorption–desorption kinetics of CO₂ on Rh surfaces has been studied and reported, albeit in ideal situations such as on single-crystal surfaces [25]. The surface structure of the washcoated Rh catalysts used in the present experiments are randomly oriented and with surface defects (e.g., kinks, ledges, etc.). Because CO₂ is only weakly adsorbed on Rh, the surface kinetics is affected significantly by small variations in surface structure. Thus, it is reasonable to consider the rate expressions for Reactions 5 and 11 as parameters that can be varied to represent measured results.

The reaction mechanism (Table 1) is written as pairs of irreversible reactions. However, the forward and reverse rates are established so as to approximately preserve microscopic reversibility, and hence enforce asymptotic approach to thermodynamic equilibrium. Although thermodynamic properties for surface species are not explicitly specified, the self-consistent forward and reverse rate expressions implicitly fix thermodynamic properties for all participating species. When an activation energy is altered for a certain reaction (i.e., CO₂ desorption, Reaction 11), the temperature-dependent thermodynamic properties for CO₂* are also de-facto altered. Because the microscopic reversibility of other reaction pairs (e.g., Reactions 21 and 22) also involve CO₂*, these reaction rates must also vary to assure reversibility considering the de-facto CO₂* properties that result from altering Reaction 11. In the present case, because of the high activation energies for Reactions 21 and 22, altering the activation energy for Reaction 11 has minimal influence on the effective reversibility of Reactions 21 and 22. Thus, the rates for Reactions 21 and 22 are unaltered from the Hartmann et al. [18] mechanism.

5. Results and discussion

5.1. Physical characterization of catalyst and support

A secondary electron detector is used in the SEM to examine catalyst-support morphology. As shown in Fig. 3, the Sr-substituted

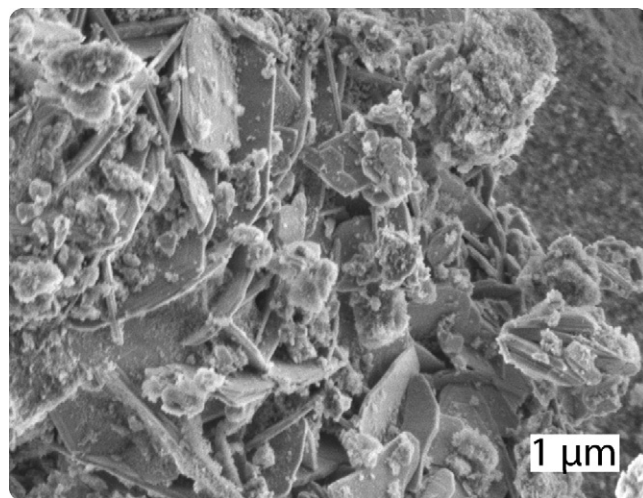


Fig. 3. Typical scanning electron micrograph of a Sr-based hexaaluminate sample.

hexaaluminate fabricated using the coprecipitation technique has the expected plate-like structure that indicates the presence of the hexaaluminate phase [26]. This morphology, which is caused by the large-cation substitution in the mirror planes of the hexaaluminate, contributes greatly to the stability.

The fraction of metal atoms exposed to the surface on the strontium substituted hexaaluminate support is 6.23% and the BET surface area of the support is 14.3 m² g⁻¹. Although the initial surface area is low relative to other commonly used supports, previous research has shown that this particular hexaaluminate substitution is highly stable and most effective at preserving metal surface area under reforming conditions [3].

5.2. Dry reforming—baseline conditions

Consider a baseline dry-reforming case with an inlet composition of 10% CH₄ and 15% CO₂ (balance Ar), resulting in the CO₂-to-CH₄ ratio being 1.5. Using a CO₂-to-CH₄ ratio that is greater than stoichiometric (CO₂/CH₄ = 1) avoids the coking that can occur when operating at stoichiometric conditions [4]. A net inlet flow rate of 19.5 standard liters per minute (slm) results in an inlet velocity through the porous frit of 90 cm s⁻¹. For the baseline case, catalyst surface temperature is maintained at 800 °C and reactor pressure is maintained at 40 kPa (300 Torr).

Fig. 4 shows predicted velocity and temperature profiles for the entire 1.6-cm space between the inlet frit and the catalytic surface. The catalyst surface is at the left edge of the graph ($z=0$ cm), with gases flowing from right to left. The velocity profiles vary throughout the space, with the axial velocity decreasing monotonically from inlet to surface. The scaled radial velocity $V = v/r$ reveals a viscous boundary layer adjacent to the catalytic surface ($z < 0.2$ cm). The linear scaled-velocity profile between the viscous boundary layer and the inlet frit indicates potential-flow behavior [11]. Although the velocity profiles span the entire 1.6-cm gap, the relevant thermal and chemical behavior is confined to the near-surface boundary layer within about 0.5 cm from the catalyst surface.

Fig. 5 shows measured (symbols) and predicted (lines) species boundary-layer profiles, spanning a distance of about 0.5 cm from the catalytic surface. Carbon balances for all measurements are maintained within 7%. The baseline conditions produce significant reforming activity, as evidenced by 5.5% CH₄ measured at the surface compared with 10% methane at the inlet. The model, utilizing the modified mechanism (Table 1) predicts the observed behavior.

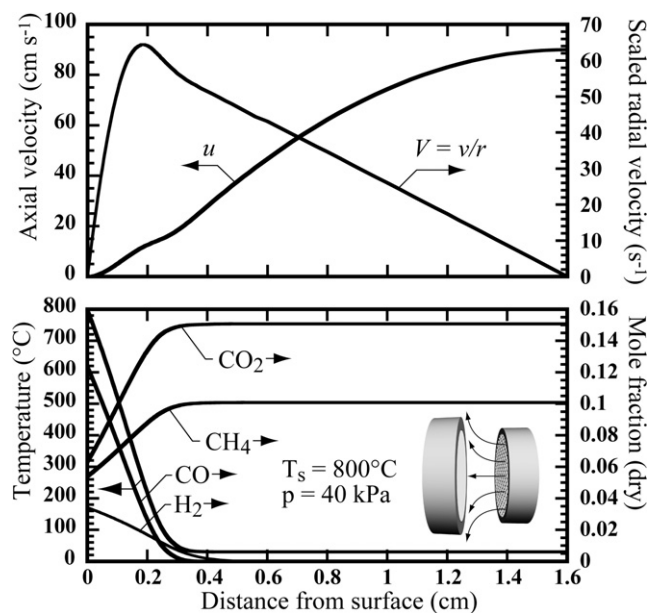


Fig. 4. Model-predicted velocity, temperature, and mole-fraction profiles for the baseline case.

While the model predictions show linear boundary profiles near the stagnation surface ($z < 0.2$ cm) the experimental data are nonlinear near the surface ($z < 0.1$ cm). Because the gas-phase chemistry is negligible at these temperatures, the boundary-layer profiles must be essentially linear in the near-surface region. The measured nonlinearity is attributed to sampling inaccuracy very near the surface. Since the sample volume is larger than the distance between the surface and the tip of the microprobe, the measurement point closest to the surface tends to preferentially sample gases farther away from the surface. This behavior is exaggerated for species profiles that have steeper gradients such as CO_2 and CO .

Assuming a global reaction and equal levels of CH_4 and CO_2 , the dry-reforming process should produce equal levels of H_2 and CO . Here, because excess CO_2 is used, the products should have relatively more CO . With excess CO_2 available, the reverse water-gas-shift process ($\text{H}_2 + \text{CO}_2 \rightarrow \text{CO} + \text{H}_2\text{O}$), tends to convert H_2 to CO . The increased $\text{CO}:\text{H}_2$ ratio in the products is observed in the results shown in Fig. 5

The modeling results depend upon knowing the value used for the effective catalyst area. Because the effective area has not been measured directly on the substrate in the stagnation-flow reactor, the effective area is taken as a parameter that is adjusted once to achieve agreement with the baseline measurements. The results shown in Fig. 5 use $F_{\text{cat,geo}} = 90$; all subsequent modeling results use

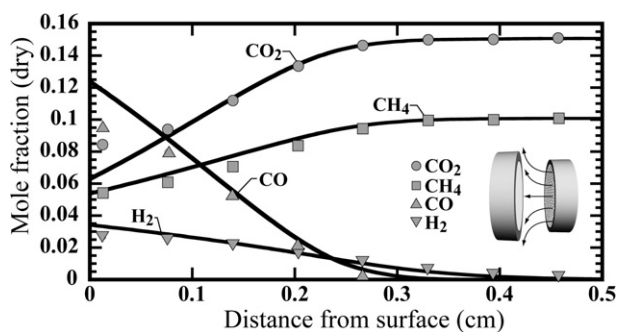


Fig. 5. Comparison of measured boundary-layer mole-fraction profiles with model predictions for a CO_2/CH_4 ratio of 1.5 and surface temperature of 800°C (baseline case).

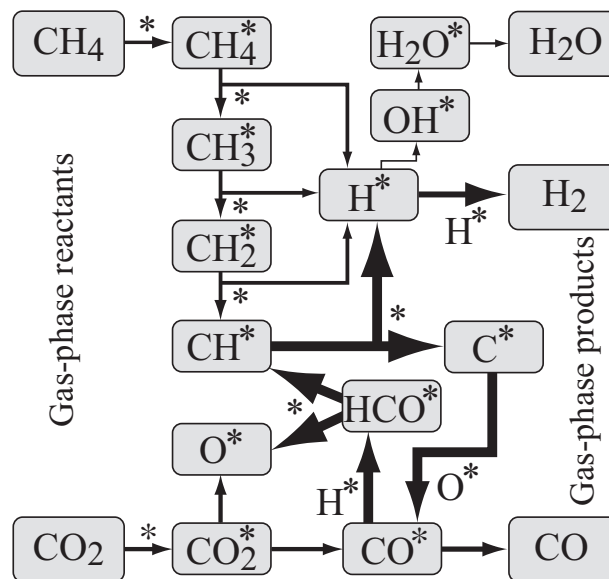


Fig. 6. Reaction-path diagram for the baseline case with $\text{CO}_2/\text{CH}_4 = 1.5$.

this value for the area ratio. This factor is in reasonable agreement with the CO pulse-chemisorption measurements on catalysts that were fabricated with similar loadings and processing techniques. The CO pulse-chemisorption measurements found $F_{\text{cat,geo}} = 56$.

5.3. Reaction pathways

The model results can be interrogated to develop a reaction-path diagram (Fig. 6) that assists in understanding the dry-reforming processes. Gas-phase reactants are shown on the left and gas-phase products are shown on the right. The center portion of the diagram shows surface species designated by an asterisk with open surface sites designated by single asterisks. The thickness of the lines connecting the species are proportional to the net reaction rates of progress. A species that is associated with a line indicates a reactant in a particular reaction.

Fig. 6 shows that dry reforming begins by adsorption of CH_4 and CO_2 onto the catalyst surface. The surface-adsorbed CH_4^* undergoes a series of hydrogen-elimination steps, ultimately leading to adsorbed atomic hydrogen H^* and carbon C^* . The adsorbed CO_2^* dissociates to O^* and CO^* . The surface species H^* , O^* , C^* , CO^* , CH^* , and HCO^* all react rapidly among themselves (thick lines). Surface C^* reacts with O^* to produce CO^* , which in turn reacts with H^* to produce HCO^* . The HCO^* dissociates to O^* and CH^* , which then participate in other fast reactions to regenerate C^* , H^* , and CO^* . Ultimately, gas-phase H_2 is formed by recombinative desorption of H^* and gas-phase CO is formed by desorption of CO^* .

The elementary pathway for oxidation of C^* by O^* agrees with several of the previously published mechanisms [6,7]. However, the origin of surface-adsorbed oxygen differs from previously published pathways. In the present mechanism, the majority of the O^* is created via the dissociation of HCO^* to CH^* and O^* (Reaction 25). Previous investigators have suggested that O^* is produced primarily by CO_2^* dissociating to CO^* and O^* [6,7]. Although the CO_2^* dissociation pathway is included in the present mechanism, results show that it is not the primary route to forming O^* . Simulations utilizing earlier mechanisms that do not include the HCO^* pathway [16,17] fail to predict the present dry-reforming measurements. Maestri et al. report that the oxidation of surface-adsorbed carbon proceeds through OH^* rather than O^* [10]. While this reaction is also included in the present mechanism, it is not predicted to be the dominant pathway for C^* oxidation under dry-reforming conditions.

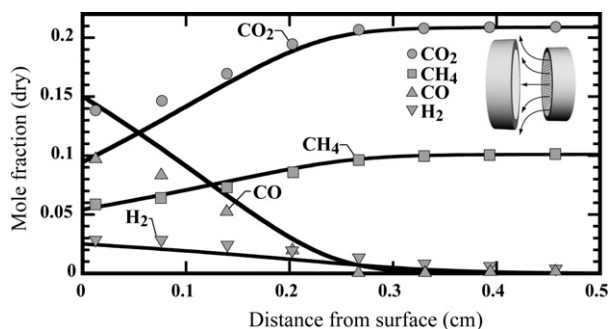


Fig. 7. Comparison of measured boundary-layer mole-fraction profiles with model predictions for an inlet CO_2/CH_4 ratio of 2.0 and surface temperature of 800 °C.

5.4. Dry-reforming at various operating conditions

After validating the model for the baseline conditions, the present work explores the fidelity of the mechanism by varying the experimental conditions and comparing the measured results to predictions using the modified reaction mechanism. In these experiments the reactor pressure is maintained at 300 Torr and the total inlet flow rate is constant at 19.5 slm.

5.4.1. Effect of CO_2/CH_4 ratio

CO_2 fractions are often increased relative to stoichiometric ratios ($\text{CO}_2/\text{CH}_4 = 1$) under dry-reforming conditions to avoid carbon formation [4]. Fig. 7 shows experimentally measured and computationally predicted species profiles when the CO_2/CH_4 ratio in the feed stream is increased from 1.5 to 2.0. The inlet composition for this case is 10% CH_4 , 20% CO_2 (balance Ar). Predictions from the modified reaction mechanism continue to agree well with measured results at increased CO_2/CH_4 ratio. At higher CO_2/CH_4 ratios, the reaction-path diagram is qualitatively similar to Fig. 6. The rates of production of surface H_2O increase slightly, presumably due to a marginal increase in surface oxygen.

5.4.2. Effect of temperature

Because most catalytic processes depend strongly upon temperature, it is important to measure and model temperature-dependent performance. The experiments presented in this section are conducted with surface temperatures ranging from 700 °C to 850 °C.

Fig. 8 illustrates the major-species profiles for three different catalytic-surface temperatures. The inlet compositions are the same as the baseline case ($\text{CO}_2/\text{CH}_4 = 1.5$). As expected, reactant (CH_4 and CO_2) conversion and syngas (H_2 and CO) production increase as functions of increasing temperature. Again, the model agrees reasonably well with the measurements. However, it appears that the net activation energy for the experimental measurements is different from predictions. This is particularly the case for the CO and CO_2 species.

Arrhenius plots of the effective CH_4 conversion provide further insight into the observed net activation energy in dry reforming. Taylor, et al. defined an effective conversion [13] using the mole fraction of methane at the surface. For methane, the conversion is defined as

$$\eta_{\text{CH}_4} = \frac{X_{\text{CH}_4, \text{inlet}} - X_{\text{CH}_4, \text{surf}}}{X_{\text{CH}_4, \text{inlet}}}, \quad (11)$$

where $X_{\text{CH}_4, \text{inlet}}$ and $X_{\text{CH}_4, \text{surf}}$ are the methane mole fractions at the inlet (i.e., unreacted feed stream) and at the surface respectively. The present effort applies this concept, but substitutes the value for $X_{\text{CH}_4, \text{surf}}$ at a distance of $z = 0.075$ cm rather than at the surface due to the measurement error at the catalyst surface.

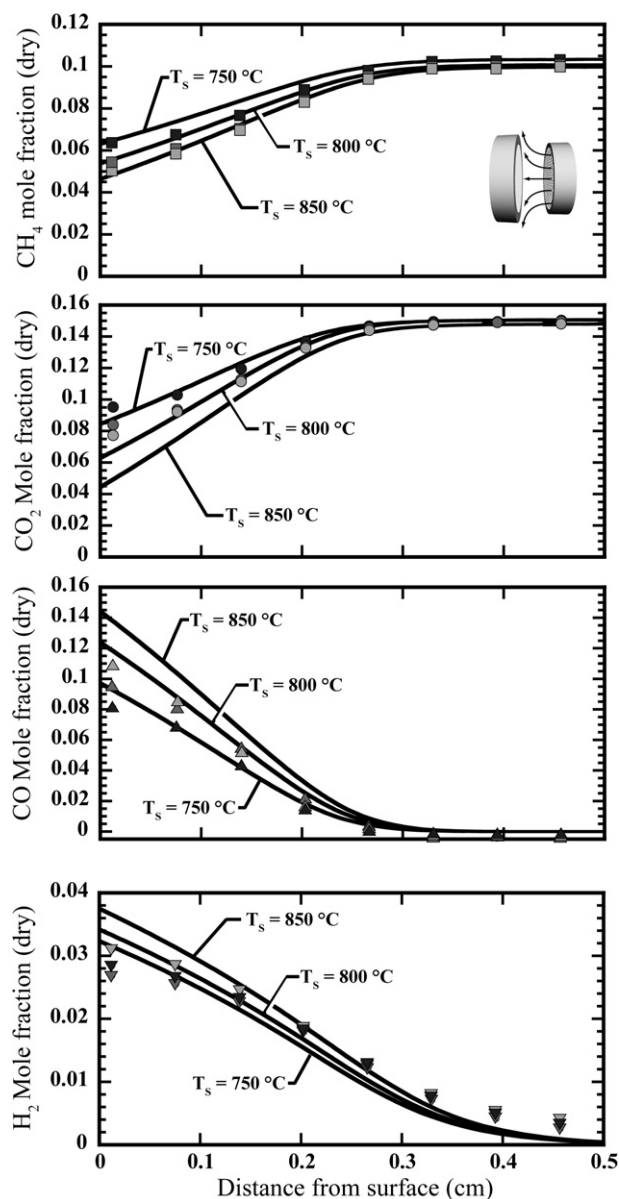


Fig. 8. Boundary layer mole fraction profiles for the major species at three different surface temperatures.

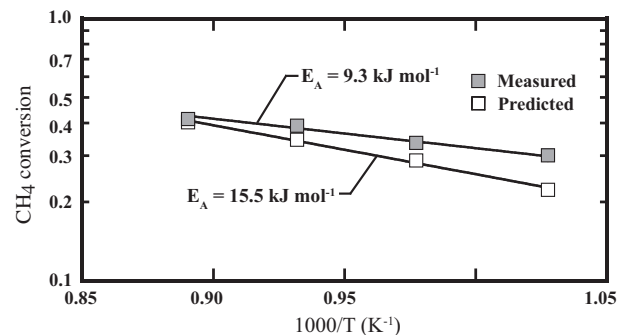


Fig. 9. Arrhenius plots for measurements and predictions based on effective methane conversion, η_{CH_4} . CO_2/CH_4 ratio is 1.5.

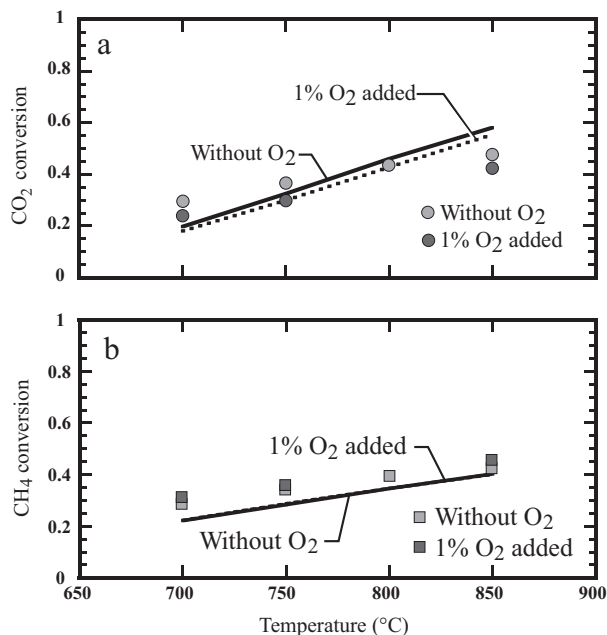


Fig. 10. Effective reactant conversions with and without oxygen addition over the surface temperature range 700 °C to 850 °C. CO₂/CH₄ ratio is 1.5.

Fig. 9 shows an Arrhenius plot of the effective methane conversion. Initial model predictions indicated a net activation energy of 19.0 kJ mol⁻¹. Because of the relative greater temperature dependence of the predicted CO₂ profiles in Fig. 8, the activation energy of the CO₂ desorption step (Reaction 11) is decreased from 21.7 kJ mol⁻¹ to 18.0 kJ mol⁻¹. The result of this change is a decrease in the predicted net activation energy to 15.5 kJ mol⁻¹. While this value moves closer to the experimental measurement (9.3 kJ mol⁻¹), the net activation energy predicted by the model remains greater than the experimental value. Further decrease of the activation energy for the CO₂ desorption step has no effect.

Similarly, the activation energy of the CH₄ desorption step (R11) was varied to decrease the modeled temperature dependence. The temperature dependence of the predicted major species profiles were insensitive to variations in the activation energy of ± 5 kJ mol⁻¹.

5.4.3. Effect of O₂ enrichment

Donazzi et al. show that incorporating low levels of oxygen can significantly increase CH₄ conversion in dry-reforming processes when the CO₂/CH₄ = 1 [27]. However, for CO₂/CH₄ ratios greater than 1, the addition of oxygen had negligible effect on conversion.

The effective conversion concept is used here to evaluate the effects of oxygen addition on methane and CO₂ conversion. Dry-reforming effective conversions are calculated at CO₂/CH₄ = 1.5, with and without 1% O₂ addition. For all cases, the 1% O₂ displaces 1% Ar. The surface temperature ranges from 700 to 850 °C. Fig. 10a shows that O₂ enrichment has little effect on carbon dioxide conversions at the conditions tested. Similarly, O₂ enrichment has a negligible effect on methane effective conversions (Fig. 10b), which is consistent with the findings of Donazzi et al. [27]. The model generally captures all the observed behaviors.

5.4.4. Comparison to previous steam-reforming data

Although the primary objective of the present paper is to investigate dry reforming, the resulting reaction mechanism must also continue to predict steam-reforming and partial-oxidation behavior. Thus, it must be assured that the changes to reaction rate parameters do not adversely affect the model's predictive ability

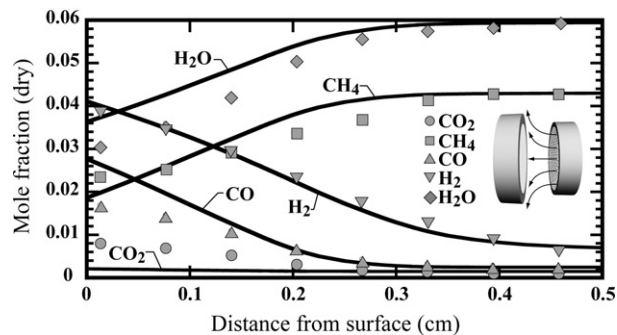


Fig. 11. Boundary-layer mole-fraction profiles measured in the stagnation-flow reactor under steam reforming conditions. Steam-to-carbon ratio is 1.4 and surface temperature is approximately 740 °C. Modeled results here are computed using the reaction mechanism presented in Table 1.

for other circumstances. In previous research, the stagnation-flow reactor was used to study methane steam reforming with similar catalysts [3] to those used in the present study. These previous data are used to evaluate the fidelity of the revised chemical mechanism for predicting steam-reforming conditions.

The experimental conditions for the baseline steam reforming case presented in the previous work were as follows. The inlet composition is 4.3% CH₄ and 5.9% H₂O (balance Ar), which is a steam-to-carbon ratio of 1.4. The surface temperature is 740 °C and the reactor pressure is maintained at 300 Torr. The total inlet flow rate is 16.4 slm resulting in an inlet velocity at the porous frit of 130 cm s⁻¹.

Fig. 11 shows experimentally measured chemical-boundary layer profiles (symbols) under steam reforming conditions from the previous publication. Also shown are the predicted species profiles (lines) computed using the elementary reaction mechanism presented in this work (Table 1). The predicted species profiles are computed using a different value of $F_{\text{cat,geo}}$ to reflect the overall activity of the previous Rh-based catalyst.

The present mechanism continues to represent the previous steam-reforming data reasonably well. The match between simulated and measured data follows the trends observed in the dry reforming boundary layers presented in Fig. 7. Specifically, overall CH₄ conversion is well predicted, as is the hydrogen production. H₂O and CO are overpredicted while CO₂ is underpredicted.

Model predictions of methane steam reforming using the modified Hartmann et al. mechanism subset (Table 1) are identical to predictions when using the unmodified Hartmann et al. mechanism [18]. In addition, the predictions are only slightly different than previously published simulations using the Deutschmann et al. mechanism [3]. It should be noted that the chemical mechanism used in the previous work lacks the HCO chemistry described in Section 4. The HCO reactions are particularly important in modeling dry reforming of methane. The steam-reforming process is relatively insensitive to the rates of the CO₂ reactions that were modified to predict dry reforming.

6. Conclusions

The primary objective of this work is to provide new dry-reforming data that can assist in extending previously published reaction mechanisms for catalytic reforming of methane. The specific catalyst considered is Rh, supported on Sr-doped hexaaluminate. The stagnation-flow reactor provides a means to measure gas-phase composition profiles immediately adjacent to the catalyst surface. Such measurements are not available in practical reactor configurations (e.g., channel monoliths or porous foams). Moreover, the stagnation-flow similarity enables efficient math-

ematical modeling of the chemically reacting boundary layers. Reaction mechanisms originally developed for catalytic partial oxidation of methane on Rh/Al₂O₃ washcoats are modified and validated by comparing measurements with model predictions. The model results are then used to assist interpretation of the fundamental reaction pathways, providing quantitative insight about the overall reforming processes.

A major difference between the present reaction pathway and previously published pathways is the origin of the O* species that oxidizes C*. In the present model, the majority of surface oxygen originates from the dissociation of HCO*. The HCO* species is formed by the reaction of CO* and H*. Others have proposed that the majority of surface oxygen is created by the dissociation of CO₂* [6,7]. Because the present pathways depend heavily on HCO*, the importance of Hartmann et al. [18] implementing elementary steps involving such species is confirmed.

Sensitivity analyses identify three elementary reactions whose rate parameters must be modified to enable accurate model predictions of our stagnation-flow experimental results. Specifically, reaction rates for the desorption of methane and for the adsorption and desorption of CO₂ require significant alteration for accurate model predictions. After modification of these reaction-rate constants, the model accurately predicts species boundary-layer profiles for the baseline experimental conditions presented in this work.

Mechanism fidelity is explored by varying a number of experimental dry-reforming conditions including CO₂/CH₄ inlet ratio, catalyst surface temperature, and oxygen enrichment. Agreement between experimental results and model predictions is generally good across all explored operating conditions. The predicted CO₂ and CO boundary-layer profiles show a stronger temperature dependence than the experimental measurements. This stronger dependence is also reflected in Arrhenius plots of the effective methane conversion.

Finally, the modified mechanism is validated against previously published experimental results for steam-reforming of methane. Model predictions for the steam-reforming cases using the modified mechanism subset presented in Table 1 are quantitatively similar to those using both the unmodified mechanism [18] and from a previously published mechanism [16]. This validation under steam-reforming conditions indicates that the steam-reforming process is relatively insensitive to the rates of the CO₂ reactions that were modified to predict dry reforming.

Acknowledgements

This work was supported by the Department of Energy, Office of Energy Efficiency and Renewable Energy, Contract Number

DE-FG36-08G088100. We gratefully acknowledge the assistance of Dr. David Wickham (Reaction Systems, LLC) in fabricating the hexaaluminate supports and Ms. Canan Karakaya (Karlsruhe Institute of Technology) for collaboration in aspects of reactor development.

References

- [1] J.R. Rostrup-Nielsen, J.-H. Bak Hansen, *J. Catal.* 144 (1993) 38–49.
- [2] J.T. Richardson, S.A. Paripatyadar, *Appl. Catal.* 61 (1990) 293–309.
- [3] N.E. McGuire, N.P. Sullivan, R.J. Kee, H. Zhu, J.A. Nability, J.R. Engel, D.T. Wickham, M.J. Kaufman, *Chem. Eng. Sci.* 64 (2009) 5231–5239.
- [4] M.C.J. Bradford, M.A. Vannice, *Catal. Rev. Sci. Eng.* 41 (1999) 1.
- [5] A. Erdohelyi, J. Cserenyi, F. Solymosi, *J. Catal.* 141 (1993) 287–299.
- [6] A.M. Efstathiou, A. Kladi, V.A. Tsipouriari, X.E. Verykios, *J. Catal.* 158 (1996) 64–75.
- [7] J. Wei, E. Iglesia, *J. Catal.* 225 (2004) 116–127.
- [8] M.F. Mark, W.F. Maier, *J. Catal.* 164 (1996) 122–130.
- [9] M. Maestri, D.G. Vlachos, A. Beretta, G. Groppi, E. Tronconi, *AIChE J.* 55 (2009) 993–1008.
- [10] M. Maestri, D.G. Vlachos, A. Beretta, G. Groppi, E. Tronconi, *J. Catal.* 259 (2008) 211–222.
- [11] R.J. Kee, M.E. Coltrin, P. Glarborg, *Chemically Reacting Flow, Theory and Practice*, Wiley, Hoboken, NJ, 2003.
- [12] O. Deutschmann, R. Schmidt, F. Behrendt, J. Warnatz, 26th Symposium on Combustion/The Combustion Institute, 1996, pp. 1747–1754.
- [13] J.D. Taylor, M.D. Allendorf, A.H. McDaniel, S.F. Rice, *Ind. Eng. Chem. Res.* 42 (2003) 6559–6566.
- [14] L.L. Raja, R.J. Kee, O. Deutschmann, J. Warnatz, L.D. Schmidt, *Catal. Today* 59 (2000) 47–60.
- [15] H. Zhu, R.J. Kee, J. Engel, D. Wickham, *Proc. Combust. Inst.* 31 (2007) 1965–1972.
- [16] O. Deutschmann, R. Schwiedernoch, L.I. Maier, D. Chatterjee, *Stud. Surf. Sci. Catal.* 136 (2001) 251–258.
- [17] R. Schwiedernoch, S. Tischer, C. Correa, O. Deutschmann, *Chem. Eng. Sci.* 58 (2003) 633–642.
- [18] M. Hartmann, L. Maier, H.D. Minh, O. Deutschmann, *Combust. Flame* 157 (2010) 1771–1782.
- [19] S.A. Seyed-Reihani, G.S. Jackson, *Chem. Eng. Sci.* 59 (2004) 5937–5948.
- [20] Gregory P. Smith, David M. Golden, Michael Frenklach, Nigel W. Moriarty, Boris Eiteneer, Mikhail Goldenberg, C. Thomas Bowman, Ronald K. Hanson, Soonho Song, William C. Gardiner Jr., Vitali V. Lissianski, Zhiwei Qin, *GRI-Mech 3.0*, http://www.me.berkeley.edu/gri_mech/.
- [21] J.F. Grcar, R.J. Kee, M.D. Smooke, J.A. Miller, *Proc. Combust. Inst.* 21 (1986) 1773–1782.
- [22] M.E. Coltrin, R.J. Kee, G.H. Evans, E. Meeks, F.M. Rupley, J.F. Grcar, Technical Report SAND91-8003, Sandia National Laboratories, 1991.
- [23] R.J. Kee, F.M. Rupley, J.A. Miller, M.E. Coltrin, J.F. Grcar, E. Meeks, H.K. Moffat, A.E. Lutz, G. Dixon-Lewis, M.D. Smooke, J. Warnatz, G.H. Evans, R.S. Larson, R.E. Mitchell, L.R. Petzold, W.C. Reynolds, M. Caracotsios, W.E. Stewart, P. Glarborg, C. Wang, O. Adigun, Technical Report Release 4.0, Reaction Design, Inc., San Diego, CA, 2005.
- [24] Q. Yan, T. Wu, L. Yang, C. Luo, W. Weng, Z. Chao, H. Wan, *J. Nat. Gas Chem.* 9 (2000) 1.
- [25] L.H. Dubois, G.A. Somorjai, *Surf. Sci.* 91 (1980) 514–532.
- [26] D. Ravichandran, S. Johnson, S. Erdei, R. Roy, W. White, *Displays* 19 (1999) 197–203.
- [27] A. Donazzi, A. Beretta, G. Groppi, P. Forzatti, *J. Catal.* 255 (2008) 259–268.